Protein MRI contrast agent with unprecedented metal selectivity and sensitivity for liver cancer imaging

Shenghui Xue[a,b], Hua Yang[c], Jingjuan Qiao[b,d], Fan Pu[b,d], Jie Jiang[b], Kendra Hubbard[b], Khan Hekmatyar[e], Jason Langley[f], Mani Salarian[b], Robert C. Long[g], Robert G. Bryant[h], Xiaoping Philip Hu[f], Hans E. Grossniklaus[c], Zhi-Ren Liu[a], and Jenny J. Yang[b,1]

Departments of [a]Biology and [b]Chemistry, Center for Diagnostics and Therapeutics, Georgia State University, Atlanta, GA 30303; Departments of [c]Ophthalmology and [g]Radiology, Emory University, Atlanta, GA 30322; [d]Inlighta Biosciences LLC, Marietta, GA 30068; [e]Complex Carbohydrate Research Center, University of Georgia, Athens, GA 30602; [f]Coulter Department of Biomedical Engineering, Georgia Tech and Emory University, Atlanta, GA 30322; and [h]Department of Chemistry, University of Virginia, Charlottesville, VA 22904

With available MRI techniques, primary and metastatic liver cancers that are associated with high mortality rates and poor treatment responses are only diagnosed at late stages, due to the lack of highly sensitive contrast agents without Gd^{3+} toxicity. We have developed a protein contrast agent (ProCA32) that exhibits high stability for Gd^{3+} and a 10^{11}-fold greater selectivity for Gd^{3+} over Zn^{2+} compared with existing contrast agents. ProCA32, modified from parvalbumin, possesses high relaxivities (r_1/r_2: 66.8 mmol^{-1}·s^{-1}/ 89.2 mmol^{-1}·s^{-1} per particle). Using T_1- and T_2-weighted, as well as T_2/T_1 ratio imaging, we have achieved, for the first time (to our knowledge), robust MRI detection of early liver metastases as small as ~0.24 mm in diameter, much smaller than the current detection limit of 10–20 mm. Furthermore, ProCA32 exhibits appropriate in vivo preference for liver sinusoidal spaces and pharmacokinetics for high-quality imaging. ProCA32 will be invaluable for noninvasive early detection of primary and metastatic liver cancers as well as for monitoring treatment and guiding therapeutic interventions, including drug delivery.

MRI | uveal melanoma | metastasis | contrast agents | T_2/T_1 ratio imaging

Tumor metastasis is the main cause of nearly all human cancer-related deaths. Liver is a common site for metastases of a variety of cancers, including melanoma, breast, pancreatic, and colon cancers (1, 2). For example, uveal melanoma, the most common primary intraocular tumor, has a 40% risk of metastasizing to the liver within 10 y of diagnosis of the primary tumor. Hepatic metastases, which occur in 95% of patients with uveal melanoma metastasis, result in death in almost all cases. This high death rate is related to the recognition of liver metastasis at a late clinical stage (at stage II or later in the TNM system) in which the metastatic uveal melanoma is resistant to currently available systemic chemotherapies (3, 4). The liver may also give rise to primary tumors such as hepatocellular carcinoma (HCC), which is the most common primary malignancy worldwide (5). However, currently there is no reliable way to detect primary liver cancer and hepatic metastases at early stages with high sensitivity and specificity.

MRI is a widely used clinical imaging modality that provides exquisite soft-tissue contrast without using ionizing radiation (6, 7). More than 35% of MRI scans use MRI contrast agents, particularly paramagnetic gadolinium (Gd^{3+})-based contrast agents, which shorten T_1 and lead to an increase in MRI intensity (8). All clinically approved Gd^{3+}-containing contrast agents are based on small chelators with relaxivity (r_1 and r_2) values around 4–6 mM^{-1}·s^{-1}. Their low relaxivities severely limit the sensitivity of current MR imaging methods with respect to detection of lesions and treatment planning and monitoring. Repeat MRI scans are frequently requested for patients with ambiguous small lesions and are used as a routine follow-up modality for high-risk patients, but they are clinically suboptimal and cost ineffective and may lead to mistreatment and metal toxicity related to the high injection doses required. Imaging of liver lesions is particularly

challenging due to rapid liver excretion of contrast agents. Detection of small liver lesions at early disease stages requires contrast agents that have a significantly improved sensitivity and a large dynamic range with reduced background water signal in tissue, as well as appropriate liver distributions and retention times for high-quality imaging. The most commonly used clinically approved T_1-weighted liver contrast agents, gadolinium–ethoxybenzyl–diethylenetriamine pentaacetic acid (Gd-EOB-DTPA) (Eovist, United States; Primovist, Europe; Bayer) and gadobenate dimeglumine (Gd-BOPTA) (Multihance; Bracco), have 50% and 5% hepatocyte uptake, respectively (9). They cannot detect early-stage small liver tumors and metastases (size, <0.5 mm), differentiate dysplastic nodules from HCC, or discriminate tumor thrombosis from platelet-fibrin thrombosis. Thus, there are pressing unmet needs for innovative MRI contrast agents with markedly improved sensitivity, metal stability, and pharmacokinetics, as well as more robust imaging methodologies to enable the earlier detection of small tumors, thereby leading to earlier diagnosis and more efficacious treatments as well as to monitor disease progression of high-risk patients.

Herein, we report the development of a protein-based MRI contrast agent, ProCA32, which has both unprecedented metal selectivity and relaxivities in r_1 and r_2, and appropriate liver retention time and distribution. It enables us to noninvasively detect micrometastatic liver tumors at early stages using T_1-weighted, T_2-weighted, or T_2/T_1 imaging as confirmed with histological analysis. Our developed protein MRI contrast agents and imaging

Significance

Primary and metastatic liver cancers that are associated with high mortality rates and poor treatment responses are only diagnosed at late stages, due to the lack of highly sensitive contrast agents and robust imaging methodologies. We have developed a protein MRI contrast agent (ProCA32) by engineering high-affinity Gd^{3+}-binding pockets in rat and human α-parvalbumin. ProCA32 can function as both a T_1- and T_2-weighted contrast agent, which enables noninvasive detection of early-stage micrometastatic liver tumors with sizes as small as 0.24 mm using T_1- and T_2-weighted or T_2/T_1 ratio MRI. Our protein-based MRI contrast agents and imaging methodology are expected to provide robust results for the early detection of liver cancer as well as other liver diseases.

BIOCHEMISTRY

methodology are expected to be robust in the early detection of primary liver cancer, liver metastasis, and other liver diseases, such as cirrhosis and liver fibrosis, and in guiding the treatment of these diseases.

Results

Design of ProCA32 with High Gd^{3+} Affinity and Metal Selectivity for Liver Imaging. One of the prerequisites for in vivo contrast agents is to have required metal stability, especially kinetic stability with high selectivity for Gd^{3+} over physiological metal ions. We previously reported that designing a Gd^{3+}-binding site into a scaffold protein CD2, named ProCA1, significantly improves relaxivity by increasing water number q ($q = 1.8$) and tuning correlation time. Although it enables molecular imaging of biomarkers such as HER2, ProCA1 has relatively low Gd^{3+} binding affinity ($K_d = 8.7 \times 10^{-13}$ M), compared with clinical MRI contrast agents [1.9×10^{-21} M for DTPA and 1.4×10^{-17} M for DTPA–bis(methylamide) (DTPA-BMA)], even though its metal selectivities for Gd^{3+} over Mg^{2+}/Ca^{2+}/Zn^{2+} are better than DTPA-BMA and Gd-DTPA (10–13). Based on our extensive studies on metal binding and the selectivity of various types of proteins with high coordination properties (10, 14), we hypothesized that strong Gd^{3+} binding affinity and metal selectivity for Gd^{3+} over physiological metal ions can be achieved by modifying the electrostatic interaction of well-coupled EF-hand calcium-binding proteins. We further reasoned that improved in vivo sensitivity of contrast agents can be achieved by increasing both r_1 and r_2. Proteins have sufficient secondary and outer hydration shells around the metal-binding site, which contribute significantly to relaxivity. It is possible to increase both r_1 and r_2 by controlling the rotational correlation time, τ_R, at around 2–6 ns at clinical field strengths (Fig. S1). One important benefit of combining T$_1$- and T$_2$-weighted imaging is improvement in contrast within the desired tissue or organ as a result of background signal suppression, leading to increased detection sensitivity (Fig. 1*A* and Fig. S2). Such an imaging strategy is not practical with clinical MRI contrast agents due to their low r_2. In fact, although the currently used clinical contrast agents have the desired r_2/r_1 ratio of 1.2, their low r_2 of 5 mM$^{-1}\cdot$s^{-1} cannot provide significant T$_2$ contrast in vivo at physiologically permitted injection doses and feasible echo times (Fig. S2).

Fig. 1*B* shows the model structure of our developed protein contrast agent (ProCA32), which was created by introducing one more negatively charged ligand S56D in the EF-hand motif 1 of rat or human α-parvalbumin to tune Gd^{3+} binding affinity and metal selectivity. Parvalbumin (ProCA30) was chosen because of its strong calcium affinity ($K_d = 8.35 \pm 0.29 \times 10^{-9}$ M; Fig. 1) and stability. An F103W mutation was introduced to allow determination of metal binding affinity by luminescence resonance energy transfer (LRET) and water number by Tb^{3+} luminescence life time decay. PEGylation of ProCA32 by TMS(PEG)12 (named as ProCA32-P40) allows us to increase blood retention time, liver preference, solubility, and stability of the designed protein (15).

Unprecedented Metal Selectivity, Stability, and Low Toxicity of ProCA32. Nephrogenic systemic fibrosis (NSF) associated with free Gd^{3+} toxicity of clinically approved contrast agents is reported to correlate with their transmetallation (16). We first examined metal binding affinity of bacterially expressed, purified, and PEGylated ProCA32 using several spectroscopic methods (*SI Materials and Methods*; Fig. 1*C* and Fig. S3 *A–E*). A Tb^{3+}-DTPA buffer system (Fig. S3 *A* and *B*) was used to control free Tb^{3+} concentration. The dissociation constant ($K_{d1} = 8.9 \times 10^{-22}$ and $K_{d2} = 1.4 \times 10^{-21}$ M by the Adair equation) between Tb^{3+} and ProCA32 was then determined by Tb^{3+}-LRET. The Gd^{3+} binding affinity (2.79×10^{-22} M) determined using competition assays (Fig. S3*C*) is comparable to that of DTPA (1.86×10^{-21} M) (Fig. 1). Importantly, ProCA32 exhibited 10^{11}- to 10^2-fold greater metal selectivity than DTPA for physiological metal ions, such as Zn^{2+}, Ca^{2+}, and Mg^{2+} (Fig. 1 and
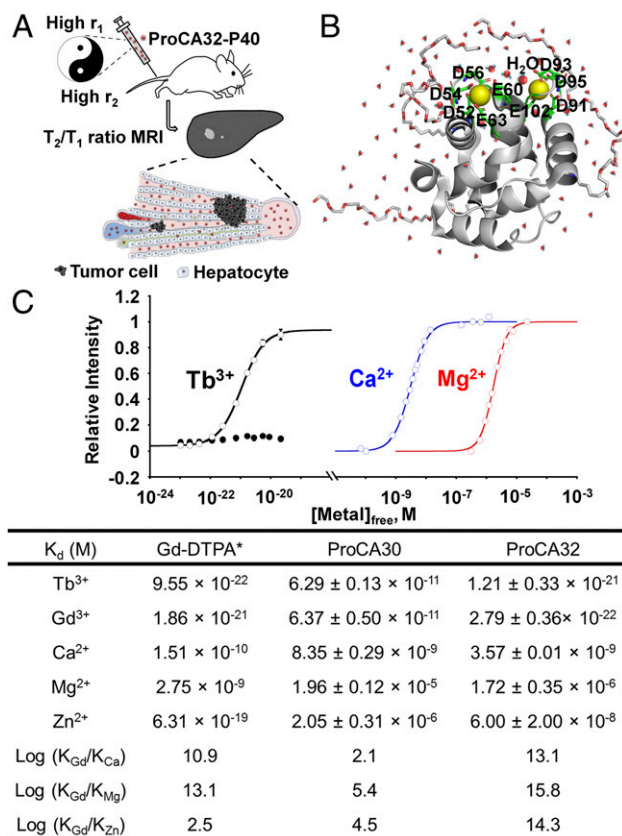

Fig. 1. Design and stability studies of ProCA32 and ProCA32-P40. (*A*) Cartoon illustration of liver tumor detection by ProCA32-P40. ProCA32-P40 has high r_1 and r_2 relaxivities. Less than 1 h after injection of ProCA32-P40, it is mainly distributed in the liver sinusoidal space and very little ProCA32-P40 are accumulated in the tumor. T$_1$-, T$_2$-weighted, and T$_2$/T$_1$ ratio imaging by MRI were used for imaging liver tumor. (*B*) The model structure of ProCA32-P40. ProCA32 was generated from parvalbumin by incorporating the S56D and F103W mutations. ProCA32-P40 was further developed by covalently linking PEG to ProCA32. The model structure of ProCA32-P40 is generated based on the structure of α-parvalbumin (Protein Data Bank ID code 1RWY). (*C*) Determination of Tb^{3+} (black; $n = 3$), Ca^{2+} (blue; $n = 3$), and Mg^{2+} (red; $n = 3$) affinities for parvalbumin mutants (○, ProCA32; ●, parvalbumin with F103W single mutation) using fluorescence spectroscopy. (Table) Metal stabilities and selectivities of DTPA (*from National Institute of Standards and Technology Standard Reference Database 46), ProCA30 ($n = 3$), and ProCA32 ($n = 3$).

K_d (M)	Gd-DTPA*	ProCA30	ProCA32
Tb^{3+}	9.55×10^{-22}	$6.29 \pm 0.13 \times 10^{-11}$	$1.21 \pm 0.33 \times 10^{-21}$
Gd^{3+}	1.86×10^{-21}	$6.37 \pm 0.50 \times 10^{-11}$	$2.79 \pm 0.36 \times 10^{-22}$
Ca^{2+}	1.51×10^{-10}	$8.35 \pm 0.29 \times 10^{-9}$	$3.57 \pm 0.01 \times 10^{-9}$
Mg^{2+}	2.75×10^{-9}	$1.96 \pm 0.12 \times 10^{-5}$	$1.72 \pm 0.35 \times 10^{-6}$
Zn^{2+}	6.31×10^{-19}	$2.05 \pm 0.31 \times 10^{-6}$	$6.00 \pm 2.00 \times 10^{-8}$
Log (K_{Gd}/K_{Ca})	10.9	2.1	13.1
Log (K_{Gd}/K_{Mg})	13.1	5.4	15.8
Log (K_{Gd}/K_{Zn})	2.5	4.5	14.3

Fig. S3 *D* and *E*). Additional transmetallation experiments further supported the conclusion that ProCA32 has significantly higher kinetic stability and metal selectivity for Gd^{3+} over Zn^{2+} than those of Omniscan, Eovist, and Magnevist (Fig. S3*F*). To our knowledge, ProCA32 has the greatest metal selectivity [log (K_{Gd}/K_{Zn})] among all reported Gd^{3+}-based contrast agents (Fig. 1). Furthermore, ProCA32 also has a strong proteolytic stability, as revealed by its structural integrity for greater than 12 d of incubation in mouse serum (Fig. S3*G*). In addition, ProCA32 did not exhibit any cytotoxicity (Fig. S4*A*), acute toxicity to organs (Fig. S4*B* and Table S1), and had reduced free Gd^{3+} accumulation in mouse tissues compared with Gd-DTPA at its clinical injection dosage or GdCl$_3$ 14 d after i.v. injection (Fig. S4*C*).

Unique High r_1 and r_2 Relaxivities of ProCA32. We measured longitudinal and transverse relaxivities (r_1 and r_2) of the designed protein (Fig. 2). ProCA32, with or without PEGylation, exhibited similar per Gd r_1 relaxivities of 33.4 mM$^{-1}\cdot$s^{-1} at 37 °C and 1.4 T, which were ~10-fold greater than that of clinically approved contrast agents at 1.4 T (Fig. 2*C*). The per-Gd r_2 of ProCA32 was
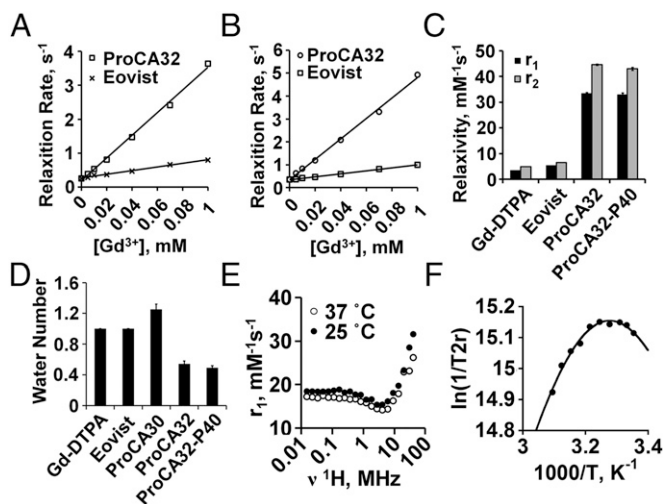
Fig. 2. Relaxivities (r_1 and r_2) and water number of protein-based MRI contrast agents. (*A*) Changes in R_1 relaxation rate over various concentrations of Gd^{3+} in ProCA32 and Eovist at 1.5 T and 37 °C. (*B*) Changes in R_2 relaxation rate over various concentrations of Gd^{3+} in ProCA32 and Eovist at 1.5 T and 37 °C (the images in *A* and *B* are representative of three independent experiments). (*C*) Per-Gd r_1 and r_2 relaxivities of Gd-DTPA ($n = 3$), Eovist ($n = 3$), ProCA32 ($n = 3$), and ProCA32-P40 ($n = 3$) at 1.5 T and 37 °C. Data are expressed as mean ± SD. (*D*) Water number of Gd-DTPA, Eovist, ProCA30 ($n = 3$), ProCA32 ($n = 3$), and ProCA32-P40 ($n = 3$). Data are expressed as mean ± SD. (*E*) NMRD profile of ProCA32-P40 measured at 37 °C and 25 °C. ν ^{1}H stands for proton Larmor frequency. (*F*) Plot of $\ln(1/T_{2r})$ versus 1,000/T of ProCA32-P40 measured by variable-temperature ^{17}O NMR. Conditions: [ProCA32-P40] = 10 mM loaded with 20 mM Gd^{3+}; pH 7.0; curve fit: $\Delta H^{\ddagger} = 25.6$ kJ·mol^{-1}, $A = 2.3 \times 10^9$, $k_{ex}^{298} = 5.4 \times 10^6$ s^{-1}.

44.6 mM^{-1}·s^{-1} at 37 °C and 1.4 T, which was at least five times higher than that of clinically approved MRI contrast agents, such as Eovist. Remarkably, ProCA32 retains r_1 of 21.9 mM^{-1}·s^{-1} at room temperature and 4.7 T, and r_2 is 56.9 mM^{-1}·s^{-1}; r_1 is 18 mM^{-1}·s^{-1} at 7 T (Table S2), which is not predicted by the usual relaxation equations (17, 18). In addition, 5 μM ProCA32 is able to generate a level of contrast similar to 50 μM Eovist with T_1-weighted spin echo and at 4.7 T (Fig. S5A). ProCA32 is able to create a significant T_2-weighted contrast at 75 μM, whereas 150 μM Eovist failed to produce any T_2 effect (Fig. S5B).

Luminescent lifetime measurements of the number of first coordination water molecules on Tb^{3+} yields a value of 0.5 per Gd (Fig. 2D) with two Gd^{3+} per protein. This result is consistent with the addition of a chelating residue in the S56D mutation saturating the first coordination sphere of one Gd^{3+} site (EF-hand 1). Based on differential metal-binding capabilities of the two metal-binding sites ($K_{d1} = 8.9 \times 10^{-22}$ and $K_{d2} = 1.4 \times 10^{-21}$ M for Tb^{3+}) and their strong cooperativity as well as similar pattern of nuclear magnetic relaxation dispersion (NMRD) profiles for metal complex ratios of 1:1 and 1:2, we concluded that Gd^{3+} initially binds to both sites partially with a strong preference for EF-hand 1 due to its stronger metal binding affinity.

The relaxation dispersion profiles shown in Fig. 2E are characteristic of Gd^{3+} coordinated to a protein. The rise in the relaxation rate constant derives from the magnetic field dependence of the electron spin-lattice relaxation rate, which decreases with increasing magnetic field; as a consequence, the effective correlation time for the electron–nuclear coupling, which includes correlation time contributions from rotation, chemical exchange, and electron relaxation, increases with increasing field. At higher field strengths, the nuclear spin-lattice relaxation rate constant generally drops to a very low value but the transverse relaxation rate becomes larger until the effective correlation time is limited by either rotational mobility of the metal center or the water exchange rate, which was measured in

ProCA32-P40 using ^{17}O NMR ($k_{ex} = 5.44 \times 10^6$ s^{-1}; Fig. 2F). The present data are unusual because the high-field r_1 remains larger than expected based on approximate models such as Solomon–Bloembergen–Morgan theory for first coordination sphere water exchange.

Several sources for the large high-field r_1 are possible: (*i*) unbound paramagnetic centers in solution (eliminated by chemical analysis), (*ii*) dipolar coupling of non-metal-protein–bound water molecules to the paramagnetic centers (19), and (*iii*) translational diffusion of water close to the paramagnetic centers in the protein interface region. Water molecules rigidly bound to the protein may contribute to relaxation by dipolar coupling to the metal centers; however, the contribution will disperse with the rotational correlation time of the protein. To maintain high-field relaxivity, there would have to be significant local motion in the bound site providing a shorter correlation time for the coupling (20). If there are many sites and a distribution of local correlation times, the magnetic field dependence may be weak and the high-field r_1 significant. Diffusive motion of water adjacent to the paramagnetic centers also contributes to the high-field relaxivity; however, the contribution is expected to be small for an unmodified protein surface because the correlation times are in the range of tens of picoseconds (19, 21). However, modification with PEG may slow this motion and amplify the contribution.

Robust Liver Preference, Significantly Improved Pharmacokinetics, Detection Limit, and Dose Efficiency of ProCA32-P40.

ProCA32-P40 has an elimination half-life time of 2.8 h in mouse compared with the value of ∼20 min for DTPA (Fig. 3A). It provides an excellent MRI enhancement of mouse blood vessel, liver, and kidney in T_1-weighted 3D gradient echo images at 4.7 T (Fig. 3B and Movie S1) even at 50 min after injection, whereas Eovist or Gd-DTPA failed to produce any pronounced enhancement at time
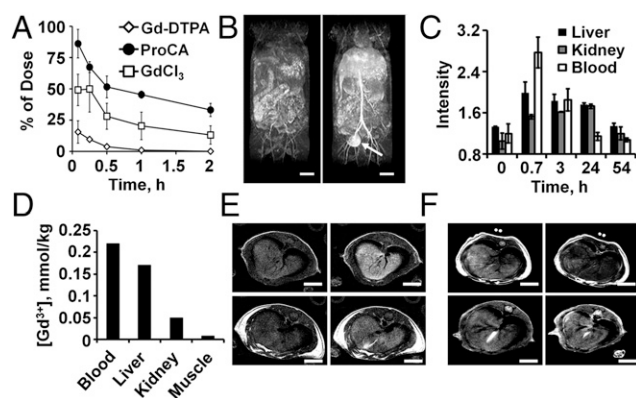

Fig. 3. Studies of the pharmacokinetics, biodistribution, and MR imaging capacity of ProCA32-P40. (*A*) Percentage of injection dose of Gd^{3+} in serum collected after injection of ProCA32-P40 (labeled as ProCA; $n = 5$), GdCl$_3$ ($n = 5$), and Gd-DTPA ($n = 5$) at different time points measured by ICP-OES at 342 nm. (*B*) Maximum intensity projection T_1-weighted MRI of mice before (*Left*) and 50 min after injection of ProCA32-P40 (*Right*). The enhancement in bladder is indicated by an arrow. (*C*) MRI signal intensity of liver ($n = 5$), kidney ($n = 5$), and blood ($n = 5$) in mice after injection of ProCA32-P40 and measurement at various time points using ImageJ. (*D*) Gd^{3+} concentration in blood, liver, kidney, and muscle after injection of ProCA32-P40 for 40–50 min measured by ICP-OES at 342 nm ($n = 3$). (*E*) T_1-weighted MRI of the mice liver before (*Left Top, Left Bottom*) and after injection of ProCA32-P40 (*Right Top*) or Eovist (*Right Bottom*). ProCA32-P40 generates a greatly enhanced liver image compared with that of Eovist in T_1-weighted MRI. (*F*) T_2-weighted MRI of mouse liver sections before (*Left Top, Left Bottom*) and after injection of ProCA32-P40 (*Right Top*) or Eovist (*Right Bottom*). ProCA32-P40 generates decreased liver intensity in T_2-weighted MRI, whereas Eovist does not cause any decrease in T_2 intensity in the same MRI sequence. [Scale bars: 5 mm (*B, E, F*).]

Xue et al.

BIOCHEMISTRY

points longer than 30 min. At 40–50 min after injection, ProCA32-P40 is mainly present in the bloodstream and extracellular extravascular spaces of liver and kidney (0.13 L/kg of volume distribution) with the highest MRI signal enhancement in these organs, and then returns to baseline at longer time as demonstrated by analyses from MRI and inductively coupled plasma optical emission spectrometry (ICP-OES) (Fig. 3 *B–D*). Results from both T_1-weighted 3D gradient echo imaging and ICP-OES suggest that ProCA32-P40 is partially excreted through the kidney with great enhancement of the bladder at 50 min (Fig. 3*B*) and via the liver based on the presence of Gd^{3+} in feces (Fig. S5*C*). Approximately 60% and 30% of ProCA32-P40 were excreted from kidney and liver, respectively, 4 d after injection (Fig. S5*D*). Intact ProCA32-P40 was detected by immunoblot in feces (24 h after injection) (Fig. S5*E*), suggesting that ProCA32-P40 does not break down in liver and kidney and Gd^{3+} and the protein form a complex during excretion. Strikingly, we are able to obtain MRI enhancement of mouse kidney at an injection concentration of 0.8 μmol/kg, 100 times lower than that of clinical injection dosage of Gd-DTPA. Injection of 1.6 μmol/kg Gd-DTPA fails to provide any significant kidney MRI enhancement at the same injection dosage (Fig. S5 *F and G*).

High-quality liver MR images have been acquired using both T_1- and T_2-weighted sequences. With 0.025 mmol/kg injection dose, ProCA32-P40 exhibits a 78 ± 15% increase in the T_1-weighted signal and a 22 ± 3% decrease in the T_2-weighted signal (Fig. 3 *E* and *F*) at 4.7 T, whereas Eovist has a 39 ± 7% signal increase in the T_1-weighted image and fails to provide any change in the liver signal in T_2-weighted MRI. Thus, ProCA32-P40 has significantly improved in vitro and in vivo detection sensitivity and dose efficiency for both T_1- and T_2-weighted MRI compared with Eovist. Furthermore, in contrast to the short imaging window for clinical MRI contrast agents, such as Eovist, ProCA32-P40 enhances the entire liver for at least 3 h, which substantially widens the MRI detection window for high-quality imaging of liver, allowing us to introduce T_1-, T_2-weighted and T_2/T_1 ratio imaging, leading to a further increase in sensitivity. Using fluorescence imaging and antibody staining, as well as ICP-OES to monitor ProCA32-P40 distribution (Fig. S5 *H and I*) (see Fig. 6*H*), we further show that ProCA32 largely distributes in the sinusoidal spaces of normal liver with a significantly longer retention time than Eovist or Multihance.

In Vivo T_1-, T_2-Weighted and T_2/T_1 Ratio Imaging of Implanted and Metastatic Liver Tumors. It is known that most liver diseases, including various types of cancers in the liver, such as HCC and metastases, have altered sinusoidal architecture and blood distribution (22). In addition, we demonstrate that hepatic metastases of uveal melanoma cells have significantly reduced hepatic distribution of both ProCA32-P40 and Eovist due to disruption of the sinusoid vascular network and lack of uptake by uveal melanoma cells (Fig. S5 *H–J*) (22). Moreover, liver metastases of uveal melanoma have significantly lower ProCA32-P40 distribution than that in surrounding liver tissue as revealed by ICP-OES (Fig. S5*K*) and fluorescence imaging (Fig. S5*I*). Such a unique property allows us to test our hypothesis that ProCA32-P40 has an enhanced capacity to detect small lesions, owing to its unique high relaxivities in both r_1 and r_2 and its differential distribution in liver lesions and normal liver tissue using both T_1- and T_2-weighted imaging, and combining them using ratio imaging in both implantation (Fig. 4) and metastasis (Fig. 5) models.

Fig. 4 shows that the transplanted uveal melanoma in the liver appears brighter in T_2-weighted images due to specific signal reduction in surrounding normal liver tissue after i.v. injection of ProCA32-P40. On the other hand, the transplanted uveal melanoma in the liver appears darker in T_1-weighted imaging due to signal enhancement in surrounding normal liver tissue. Taking the ratio, T_2/T_1 effectively combines the contrasts between the
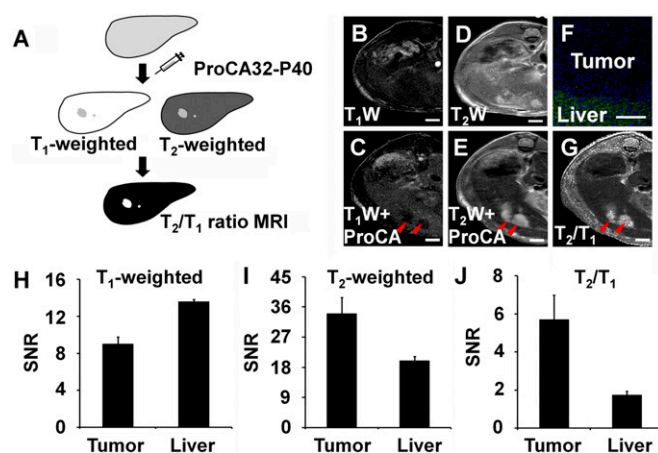

Fig. 4. Imaging of implanted liver tumor using ProCA32-P40. (*A*) Cartoon illustration of detection of liver tumors by ProCA32-P40. Because of the different distribution of ProCA32-P40 between liver and tumor, tumors show hypointensity in T_1-weighted MRI and hyperintensity in T_2-weighted MRI. The MRI signal differences between liver and tumor were further improved in T_2/T_1 ratio imaging, which is generated by dividing the intensity of T_2-weighted MRI by the intensity of T_1-weighted MRI in each corresponding pixel. (*B* and *C*) T_1-weighted MRI of tumor implanted liver before (*B*) and after (*C*) injection of ProCA32-P40. (*D* and *E*) T_2-weighted MRI of tumor implanted liver before (*D*) and after (*E*) injection of ProCA32-P40. (*F*) Immunofluorescence staining shows that ProCA32-P40 (green) has a high distribution in liver and a low distribution in tumor. (*G*) The T_2/T_1 ratio imaging of the tumor implanted liver. Tumor locations in *C*, *E*, and *G* are pointed out by red arrows. (*H*) Signal-to-noise ratio (SNR) of tumor (*n* = 5) and liver (*n* = 5) after injection of ProCA32-P40 in T_1-weighted MRI. (*I*) SNR of tumor (*n* = 5) and liver (*n* = 5) after injection of ProCA32-P40 in T_2-weighted MRI. (*J*) SNR of tumor (*n* = 5) and liver (*n* = 5) after injection of ProCA32-P40 in T_2/T_1 ratio MRI. [Scale bars: 3 mm (*B–E* and *G*) and 100 μm (*F*).]

tumor and normal liver as it decreases the liver signal and improves the homogeneity of liver signal.

Using our established mouse ocular melanoma metastasis model (23, 24), we showed that tail vein injection of ProCA32-P40 enables us to observe more than 10 hypointense lesions using T_1-weighted spin echo images (Fig. 5*D* and Fig. S6) and hyperintense lesions with sizes ranging from 0.24 to 2 mm in T_2-weighted fast spin echo images (Fig. 5*E* and Fig. S6). In contrast, these liver metastases of uveal melanoma were not detectable either without ProCA32-P40 or with injection of Eovist (Fig. S7). Furthermore, in the metastasis model, use of the T_2/T_1 ratio efficiently suppresses the liver signal, improves the homogeneity of the liver signal, and improves the contrast-to-noise ratio between liver and tumor from 3.58 ± 0.45 in T_1-weighted images and 4.33 ± 1.15 in T_2-weighted images to 5.05 ± 1.36 in T_2/T_1 ratio images (Fig. 5*F* and Fig. S6).

Histological Validation of Metastatic Lesions in Liver. Next, we performed detailed histological analysis of the uveal melanoma biomarker S100 (Fig. 6*A*), bright-field imaging of melanin (Fig. 6*B*), immunofluorescence staining (Fig. 6 *C–H*), and H&E staining (Fig. 6*J*) to confirm the identity of the liver metastatic melanoma tumors detected by MRI. ProCA32-P40 staining in tumors colocalized with CD31 immunostaining of vascular channels, indicating that ProCA32-P40 is restricted to the distribution of blood vessels in the tumor (Fig. 6 *E–G*). Consistent with the differences in contrast between tumor and liver observed using MRI, immunofluorescence staining confirms that ProCA32-P40 is mainly distributed in the sinusoidal space of the liver and has an extremely low distribution in tumor tissue (Fig. 6 *C* and *D*). Such a low distribution in tumor is dramatically different from that of the liver (Fig. 6*H*). Furthermore, we did a correlation study between H&E staining and MRI. There is an excellent correlation ($R^2 = 0.92$) between
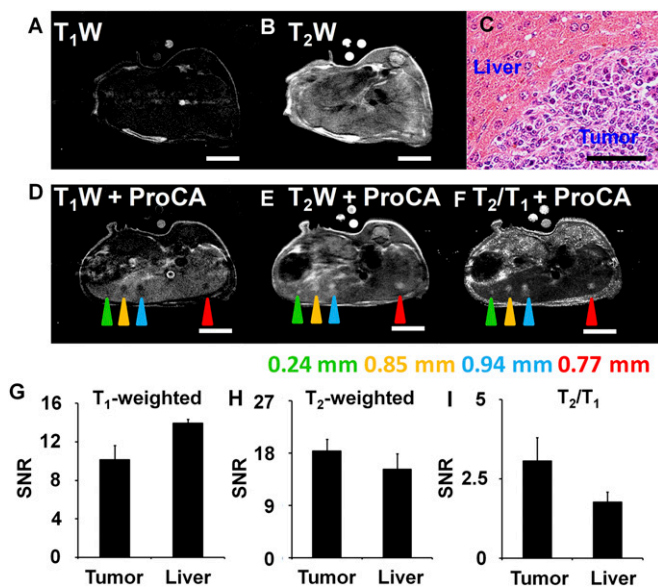
Fig. 5. Detection of metastatic uveal melanoma in liver by ProCA32-P40 using T_1-weighted (*A* and *D*), T_2-weighted (*B* and *E*), and T_2/T_1 ratio imaging (*F*) using ProCA32-P40. Metastatic uveal melanoma cannot be detected in T_1- (*A*) or T_2-weighted MRI (*B*) without injection of ProCA32-P40. Metastatic uveal melanoma (indicated by arrows) with size larger than 0.24 mm (green arrow) can be detected by T_1-weighted (*D*), T_2-weighted (*E*), and T_2/T_1 ratio imaging (*F*) after injection of ProCA32-P40. (*C*) The tumors detected by MRI were confirmed by H&E staining. (*G*) SNR of metastatic uveal melanoma (*n* = 5) and liver (*n* = 5) after injection of ProCA32-P40 in T_1-weighted MRI. (*H*) SNR of metastatic uveal melanoma (*n* = 5) and liver (*n* = 5) after injection of ProCA32-P40 in T_2-weighted MRI. (*I*) SNR of metastatic uveal melanoma (*n* = 5) and liver (*n* = 5) after injection of ProCA32-P40 in T_2/T_1 ratio MRI. [Scale bars: 5 mm (*A*, *B*, and *D–F*) and 100 μm (*C*).]

noninvasive detection by MRI with ProCA32-P40 and H&E histological analysis of all stages of metastatic lesions of uveal melanoma of varying sizes (Fig. 6 *I–K*). Thus, ProCA32-P40 enables noninvasive early detection of lesions as small as 0.24 mm, or stage I, metastatic liver tumors, which are ~100-fold smaller than the current detection threshold of >10–20 mm for stage II or later. It is also important to note that the combination of T_1-, T_2-weighted and ratio images significantly increased the confidence for detecting metastases, while reducing detection limits of liver lesions by 100-fold.

Discussion

These results demonstrate the feasibility of developing a protein MRI contrast agent, ProCA32, by protein design and modification with significantly improved r_1 and r_2. ProCA32 has unprecedented metal selectivity and improved blood, liver, and kidney pharmacokinetics. We have shown proof-of-concept that ProCA32 can be used to detect hepatic metastases of uveal melanoma at an early stage with high sensitivity.

To address a critical, unmet medical need, we developed a strategy in our creation of an MRI contrast agent using protein design and modification to increase relaxivity without compromising metal binding affinity/stability, selectivity, and pharmacokinetic properties that are dramatically different from previously reported approaches (25–32). Building on our previous success in improving relaxivity by designing a Gd^{3+}-binding site into a scaffold protein CD2 and with a goal of improving metal binding affinity, we report a method to develop the protein contrast agent ProCA32 by converting the natural Ca^{2+}-binding protein, parvalbumin, into a Gd^{3+}-binding protein that is also PEGylated. We have simultaneously achieved significantly increased longitudinal and transverse

relaxivities, Gd^{3+} binding affinity, and in vivo pharmacokinetics required for earlier detection of small lesions. ProCA32 exhibits a Gd^{3+} dissociation constant comparable to that of DTPA of 1.86×10^{-21} M, whereas wild-type parvalbumin was reported to have a Gd^{3+} affinity of 0.5×10^{-11} M (33). ProCA32 achieves metal selectivity for Gd^{3+} over Ca^{2+}, Mg^{2+}, Zn^{2+}, and other physiological metal ions that are >100- to 10^{11}-fold higher than DTPA. ProCA32 exhibits undetectable acute toxicity, cytotoxicity, and strong serum stability and low 14-d residual content in mouse bone. Taken together with its improved dose efficiency, ProCA32 is likely to significantly reduce the NSF risk associated with metal toxicity.

ProCA32 exhibits several unique relaxation properties compared with previously reported contrast agents. ProCA32 has significantly increased r_1 and r_2 with per-Gd relaxivities about 10-fold greater than Eovist at 1.4 T, permitting acquisition of both positively and negatively enhanced liver images at physiologically achievable concentrations in the liver using T_1- and T_2-weighted pulse sequences, respectively. Combining the contrasts in T_1- and T_2-weighted images obtained by using the ratio, ProA32-P40 enables a 100-fold increase in its detection limit for identifying lesions compared with existing agents (Fig. 5). In addition, the injection dosage of ProCA32-P40 at 4.7 and 7 T is comparable with clinically used protein drugs, such as Avastin. Because relaxivity of ProCA32-P40 at medical-related field strength such as 1.5 T is 50% greater than at 4.7 T (Table S2), the required injection dose efficiency of our contrast agents is expected to be increased significantly at clinical field strength. Thus, ProCA32-P40 has great potential for clinical translation.
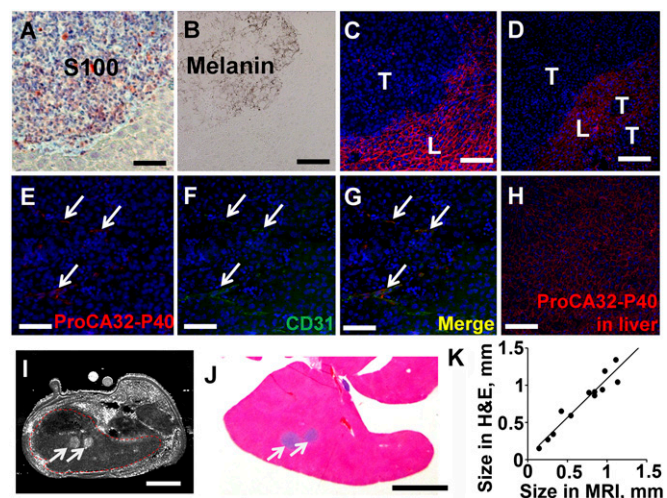

Fig. 6. Histological confirmation of metastatic uveal melanoma in liver detected by MRI. (*A*) Immunohistochemical staining of metastatic melanoma in liver using S100 antibody. (*B*) Bright-field imaging of metastatic melanoma in liver. Melanin in uveal metastatic melanoma exhibits black color. (*C* and *D*) Immunofluorescence images of ProCA32-P40 (red) distribution between metastatic melanoma and liver tissue. ProCA32-P40 was mainly distributed in liver tissue. (*E*) Immunofluorescence images of ProCA32-P40 (red) in metastatic melanoma. ProCA32-P40 has limited distribution in tumor tissue. (*F*) CD31 (green) staining of blood vessels in metastatic melanoma tissue. (*G*) Colocalization of ProCA32-P40 (red) and CD31 (green) in metastatic melanoma tissue indicates that the distribution of ProCA32-P40 is restricted to the tumor blood vessel. (*H*) Immunofluorescence images of ProCA32-P40 (red) in normal liver tissue. ProCA32-P40 largely distributes in the sinusoidal space of normal liver within 1 h after tail vein injection of ProCA32-P40. (*I*) T_2/T_1 ratio MRI of metastatic melanoma (arrow) in liver after injection of ProCA32-P40. (*J*) H&E staining of metastatic melanoma (arrow) in the liver tissue. (*K*) The correlation between MRI and H&E staining. The tumor sizes detected in MRI (*x* axis) and H&E staining (*y* axis) show very good correlation ($y = 1.04x + 0.05$; $R^2 = 0.92$). [Scale bars: 100 μm (*A–H*) and 5 mm (*I* and *J*).]

Xue et al.

PEGylation of ProCA32 increases preferential liver distribution and improves the blood retention time to a half-life of 2.8 h in vivo, in addition to enhancing protein stability and improving pharmacokinetics with a resultant increase in dose efficiency. As shown in Fig. 6H, ProCA32-P40 is mainly distributed in the sinusoidal spaces of the liver, and hepatocyte uptake is absent within 1 h after injection. These improved in vivo properties substantially widen the MRI detection window and are essential for achieving high-quality imaging with high resolution. ProCA32-P40 has a high liver retention time with a blood half-life of 2.8 h, which allows the collection of both T_1- and T_2-weighted images and an associated significant change of liver signal after one injection of ProCA32-P40 (Fig. 3). Importantly, our imaging methodologies provide additional verification for signal detection by doubling detection confidence. On the other hand, iron oxide-based nanoparticles, such as super paramagnetic nanoparticles, generate negative contrast in liver T_2- or T_2^*-weighted MRI and accumulate in the sparsely distributed Kuppfer cells of the reticuloendothelial system within a few minutes after injection, instead of in hepatocytes or the sinusoidal space.

ProCA32-P40 has the potential to fill a major gap in clinical MRI applications by enabling noninvasive and early detection of primary liver tumors and metastases, improving treatment effectiveness by targeted therapy, and guiding treatment and drug delivery. Because many liver diseases, including liver cancers such as HCC and liver metastasis from breast, brain, and colon cancer, as well as fibrosis and cirrhosis, have altered liver vascular architecture, it is expected that ProCA32-P40 can be widely used for the diagnosis of various types of diseases in the liver, including cirrhosis, fibrosis, hepatitis B virus infection, hepatitis C virus infection, alcoholism, fatty liver disease and other nonalcoholic liver disease. Improved detection sensitivity enables better delineation of tumor margins and may facilitate image-guided interventions and early intervention by providing an enhanced capacity to monitor progression in high-risk patients. To our knowledge, ProCA32 also exhibits the high per-Gd r_1 relaxivity of 18 $mM^{-1}·s^{-1}$ at high magnetic field, 7 T (Table S2) (17). Further understanding of the mechanism underlying such high relaxivities is expected to open a previously unidentified avenue to further broaden MRI applications at high magnetic fields with improved sensitivity and resolution.

Materials and Methods

Detailed descriptions of the expression, purification, PEGylation, and characterization of protein MRI contrast agents are provided in SI Materials and Methods. All animal procedures performed in this study complied with the Association for Research in Vision and Ophthalmology Statement for the Use of Animals in Ophthalmic and Vision Research and complied with an approved animal protocol from the Institutional Animal Care and Use Committee at Georgia State University and the University of Georgia. T_2/T_1 ratio images were generated using the following procedure: (i) T_1- and T_2-weighted images were acquired before and after injection of ProCA32-P40 in mice. (ii) A threshold was chosen to exclude areas of noise in the T_1- and T_2-weighted image. (iii) For each pixel with a signal intensity in the T_1-weighted image above the threshold, the corresponding pixel in the T_2-weighted image was divided by the signal intensity from the T_1-weighted image to generate new T_2/T_1 ratio image. Detailed methods, parameters, and procedures for in vivo MRI, histology analysis, biodistribution, and toxicity studies in the article are described in SI Materials and Methods.

1. Eckhardt BL, Francis PA, Parker BS, Anderson RL (2012) Strategies for the discovery and development of therapies for metastatic breast cancer. *Nat Rev Drug Discov* 11(6):479–497.
2. Van den Eynden GG, et al. (2013) The multifaceted role of the microenvironment in liver metastasis: Biology and clinical implications. *Cancer Res* 73(7):2031–2043.
3. Sato T (2010) Locoregional management of hepatic metastasis from primary uveal melanoma. *Semin Oncol* 37(2):127–138.
4. Grossniklaus HE (2013) Progression of ocular melanoma metastasis to the liver: The 2012 Zimmerman Lecture. *JAMA Ophthalmol* 131(4):462–469.
5. Arzumanyan A, Reis HM, Feitelson MA (2013) Pathogenic mechanisms in HBV- and HCV-associated hepatocellular carcinoma. *Nat Rev Cancer* 13(2):123–135.
6. Cárdenas-Rodríguez J, Howison CM, Matsunaga TO, Pagel MD (2013) A reference agent model for DCE MRI can be used to quantify the relative vascular permeability of two MRI contrast agents. *Magn Reson Imaging* 31(6):900–910.
7. Yankeelov TE, Abramson RG, Quarles CC (2014) Quantitative multimodality imaging in cancer research and therapy. *Nat Rev Clin Oncol* 11(11):670–680.
8. Major JL, Meade TJ (2009) Bioresponsive, cell-penetrating, and multimeric MR contrast agents. *Acc Chem Res* 42(7):893–903.
9. Weinmann HJ, Ebert W, Misselwitz B, Schmitt-Willich H (2003) Tissue-specific MR contrast agents. *Eur J Radiol* 46(1):33–44.
10. Yang JJ, et al. (2008) Rational design of protein-based MRI contrast agents. *J Am Chem Soc* 130(29):9260–9267.
11. Xue S, et al. (2014) Design of ProCAs (protein-based Gd^{3+} MRI contrast agents) with high dose efficiency and capability for molecular imaging of cancer biomarkers. *Med Res Rev* 34(5):1070–1099.
12. Xue S, Qiao J, Pu F, Cameron M, Yang JJ (2013) Design of a novel class of protein-based magnetic resonance imaging contrast agents for the molecular imaging of cancer biomarkers. *Wiley Interdiscip Rev Nanomed Nanobiotechnol* 5(2):163–179.
13. Qiao J, et al. (2014) Molecular imaging of EGFR/HER2 cancer biomarkers by protein MRI contrast agents. *J Biol Inorg Chem* 19(2):259–270.
14. Yang W, et al. (2005) Design of a calcium-binding protein with desired structure in a cell adhesion molecule. *J Am Chem Soc* 127(7):2085–2093.
15. Li S, et al. (2012) PEGylation of protein-based MRI contrast agents improves relaxivities and biocompatibilities. *J Inorg Biochem* 107(1):111–118.
16. Frenzel T, Lengsfeld P, Schirmer H, Hütter J, Weinmann HJ (2008) Stability of gadolinium-based magnetic resonance imaging contrast agents in human serum at 37 degrees C. *Invest Radiol* 43(12):817–828.
17. Caravan P, Farrar CT, Frullano L, Uppal R (2009) Influence of molecular parameters and increasing magnetic field strength on relaxivity of gadolinium- and manganese-based T1 contrast agents. *Contrast Media Mol Imaging* 4(2):89–100.
18. Ananta JS, et al. (2010) Geometrical confinement of gadolinium-based contrast agents in nanoporous particles enhances T1 contrast. *Nat Nanotechnol* 5(11):815–821.
19. Diakova G, Goddard Y, Korb JP, Bryant RG (2011) Water-proton-spin-lattice-relaxation dispersion of paramagnetic protein solutions. *J Magn Reson* 208(2):195–203.
20. Lipari G, Szabo A (1982) Model-free approach to the interpretation of nuclear magnetic resonance relaxation in macromolecules. 1. Theory and range of validity. *J Am Chem Soc* 104(17):4546–4559.
21. Polnaszek CF, Bryant RG (1984) Nitroxide radical induced solvent proton relaxation: Measurement of localized translational diffusion. *J Chem Phys* 81(9):4038–4045.
22. Kuruppu D, Christophi C, O'Brien PE (1997) Microvascular architecture of hepatic metastases in a mouse model. *HPB Surg* 10(3):149–157; discussion 158.
23. Yang H, et al. (2008) In-vivo xenograft murine human uveal melanoma model develops hepatic micrometastases. *Melanoma Res* 18(2):95–103.
24. Lattier JM, Yang H, Crawford S, Grossniklaus HE (2013) Host pigment epithelium-derived factor (PEDF) prevents progression of liver metastasis in a mouse model of uveal melanoma. *Clin Exp Metastasis* 30(8):969–976.
25. Winter PM, et al. (2003) Molecular imaging of angiogenesis in early-stage atherosclerosis with alpha(v)beta3-integrin-targeted nanoparticles. *Circulation* 108(18):2270–2274.
26. Guo K, et al. (2010) Near infrared-fluorescent and magnetic resonance imaging molecular probe with high T1 relaxivity for in vivo multimodal imaging. *Chem Commun (Camb)* 46(21):3705–3707.
27. Caravan P, Greenwood JM, Welch JT, Franklin SJ (2003) Gadolinium-binding helix-turn-helix peptides: DNA-dependent MRI contrast agents. *Chem Commun (Camb)* (20):2574–2575.
28. Datta A, Raymond KN (2009) Gd-hydroxypyridinone (HOPO)-based high-relaxivity magnetic resonance imaging (MRI) contrast agents. *Acc Chem Res* 42(7):938–947.
29. Shapiro MG, et al. (2010) Directed evolution of a magnetic resonance imaging contrast agent for noninvasive imaging of dopamine. *Nat Biotechnol* 28(3):264–270.
30. De Leon-Rodriguez LM, et al. (2009) Responsive MRI agents for sensing metabolism in vivo. *Acc Chem Res* 42(7):948–957.
31. Louie AY, et al. (2000) In vivo visualization of gene expression using magnetic resonance imaging. *Nat Biotechnol* 18(3):321–325.
32. Fulton DA, et al. (2006) Glycoconjugates of gadolinium complexes for MRI applications. *Chem Commun (Camb)* (10):1064–1066.
33. Cavé A, Daures MF, Parello J, Saint-Yves A, Sempere R (1979) NMR studies of primary and secondary sites of parvalbumins using the two paramagnetic probes Gd (III) and Mn (II). *Biochimie* 61(7):755–765.

Xue et al.

www.manaraa.com